ACS APPLIED MATERIALS & INTERFACES

Cite This: ACS Appl. Mater. Interfaces 2019, 11, 35977−35986

www.acsami.org

Chemically Bonding NiFe-LDH Nanosheets on rGO for Superior Lithium-Ion Capacitors

Meng Tian,[†,‡] Chaofeng Liu,[‡] Zachary G. Neale,[‡] Jiqi Zheng,[‡] Donghui Long,[*,†,§] and Guozhong Cao[*,‡]

[†]State Key Laboratory of Chemical Engineering, East China University of Science and Technology, Shanghai 200237, China

[‡]Department of Materials Science and Engineering, University of Washington, Seattle, Washington 98195, United States

[§]Shanghai Key Laboratory of Multiphase Materials Chemical Engineering, East China University of Science and Technology, Shanghai 200237, China

Supporting Information

ABSTRACT: Layered double hydroxides (LDHs) have attracted tremendous interest for applications in energy harvest and storage. However, the aggregation of nanosheets compromises the accessible active sites and limits their electrochemical performance, especially at high rates. The present study reports the synthesis of highly dispersed NiFe-LDH nanosheets anchored on reduced graphene oxide (NiFe-LDH/rGO) composites chemically bonded via a facile one-step hydrothermal method. Defect-riched rGO provides abundant active sites for heterogeneous nucleation of NiFe-LDH nanosheets, achieving the much efficient charge transfer between rGO and NiFe-LDH as compared to physically mixed NiFe-LDH + rGO. The crystallite size can effectively reduce to 5.5 nm smaller than 15.1 nm of NiFe-LDH without rGO, beneficial to expose more active surface for fast ion diffusion and redox reactions. NiFe-LDH/rGO as an anode material in lithium-ion batteries shows superior lithium storage capacity with 1202 mAh g^{-1} after 100 cycles at 100 mA g^{-1} and high-rate performance with 543 mAh g^{-1} even at 2000 mA g^{-1}. The corresponding lithium-ion capacitor with NiFe-LDH/rGO anode and mesoporous carbon microsphere cathode exhibits high energy density and power density simultaneously, with 133 Wh kg^{-1} at 25 W kg^{-1} and 4016 W kg^{-1} at 58 Wh kg^{-1}, showing the great potential for high-performance hybrid energy storage systems.

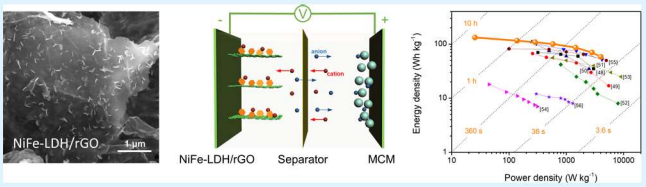

KEYWORDS: *layered double hydroxide, highly dispersed nanosheets, reduced graphene oxide, high performance, lithium-ion storage*

1. INTRODUCTION

Lithium-ion capacitors (LICs) have attracted intense attention owing to the integration of high energy densities of batteries and high power densities of supercapacitors.[1−5] Generally, LICs are fabricated by the battery-type anode achieving lithium-ion intercalation/deintercalation and the capacitor-type cathode with ion adsorption/desorption during the charge/discharge process.[6−8] The design and synthesis of suitable anode materials are crucial for LICs because the slow intercalation compared to fast ion adsorption restrains the redox process and determines the electrochemical performance of devices.[9,10] Nanostructured materials (e.g., nanospheres,[11] nanotubes,[12] nanosheets,[13] etc.) are promising candidates as anodes for lithium-ion batteries (LIBs) and LICs due to large surface area, high electrical conductivity, and enhanced intercalation kinetics. Among them, two-dimensional nanomaterials possess a layered structure with a highly exposed active surface, showing the great potential of fast ion diffusion for redox reactions, especially at high rates.[14−16]

Layered double hydroxides (LDHs) are intriguing materials with a typical two-dimensional structure, described by the general formula of $[M^{2+}_{1-x}M^{3+}_{x}(OH)_2]^{x+}(A^{n-})_{x/n}{\cdot}yH_2O$, where M^{2+} (e.g., Fe^{2+}, Co^{2+}, Ni^{2+}, Cu^{2+}, etc.) and M^{3+} (e.g., Fe^{3+}, Co^{3+}, Cr^{3+}, etc.) represent the divalent and trivalent metal cations, respectively, and A^{n-} (e.g., NO_3^-, SO_4^{2-}, Cl^-, etc.) is the interlayered anion.[17−19] Various LDHs can be easily fabricated based on different metal cations and intercalated anions, with fast ion diffusion and electron transfer, showing great potential in electrocatalysis, supercapacitors, batteries, and biotechnology.[20−24] However, the agglomeration of LDHs reduces ion diffusion rate, sacrifices accessible reaction sites, and raises large volume change, thus restricting the electrochemical performance, especially for high-rate LICs. Fabricating highly dispersed LDH sheets with a controllable nanostructure is an efficient method to accelerate the ion transportation and improve the electrochemical activity, and results in high-rate performance and great cycling stability for the desired devices.

Graphene has the advantages of large theoretical surface area (2630 $m^2 g^{-1}$), high electrical conductivity (~10^3 S m^{-1}), great mechanical flexibility, and chemical stability, providing a perfect substrate for the high-dispersed growth of nano-

Received: June 25, 2019
Accepted: September 9, 2019
Published: September 9, 2019

DOI: 10.1021/acsami.9b10719
ACS Appl. Mater. Interfaces 2019, 11, 35977−35986

Scheme 1. Schematic Illustration of Material Fabrication Processes

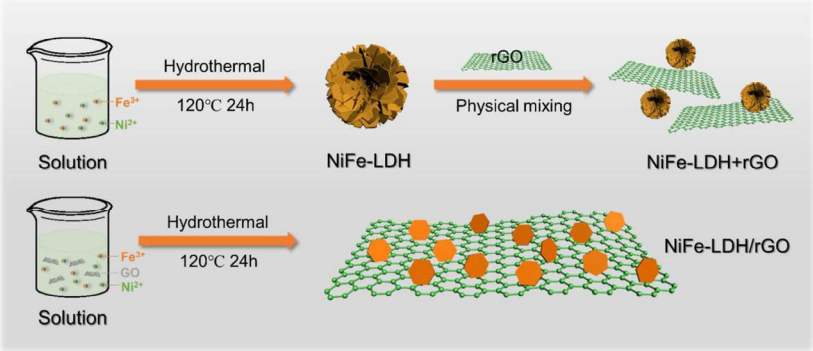

structured materials. Superior to physically mixed composites of graphene and nanomaterials, one-step chemically synthesized composites show the following advantages: (1) modifying the material nucleation by providing abundant defects and functional groups as heterogeneous nucleation sites for nanomaterial growth to buffer large volume change during the charge/discharge process; (2) establishing a high-efficiency interfacial interaction by chemical bonding between graphene and nanomaterials to facilitate charge-transfer process; and (3) displaying the synergistic effects exposing more accessible active sites of nanomaterials and graphene simultaneously.[25−27] For example, Zhou et al. studied the interfacial interaction in graphene/metal oxide systems and proposed that effective oxygen bridges between metal oxides and functional groups on graphene lead to synergistic effect and achieve lithium storage improvement.[28] Jiang et al. pointed out that the charge transfer was achieved between LDH layer and graphene, accelerating reaction kinetics and enhancing energy storage performance.[29] Therefore, chemically bonding nanomaterials on graphene can effectively modify the material nucleation, establish an interfacial chemical interaction, and improve the electrochemical properties.

Herein, we report the fabrication of NiFe-LDH/rGO with a unique structure of high-dispersed LDH nanosheets anchored on reduced graphene oxide (rGO) via a facile one-step hydrothermal method and use it as an anode material for Li-ion storage. NiFe-LDH/rGO shows an excellent interfacial interaction through oxygen bridges originated from the heterogeneous nucleation of LDH nanosheets on rGO surface. The synergistic effect reflects in the agglomeration prevention of LDH nanosheets and graphene simultaneously, thus exhibiting the greatly exposed active surface for fast redox reactions, superior to the physical mixing of NiFe-LDH and rGO (NiFe-LDH + rGO) with a weak interaction. Mesoporous carbon microspheres (MCMs) were adopted as the cathode in full LIC, prepared by a simple and efficient spray-drying method with a uniform mesoporous structure and large pore volume, beneficial to fast ion adsorption and high-rate performance. The electrochemical performance of NiFe-LDH/rGO in both half-cell and full LICs was performed, showing enhanced energy storage and excellent stability.

2. EXPERIMENTAL SECTION

2.1. Material Synthesis. All chemicals were of analytic grade purchased from Alfa Aesar and used as received without further treatment unless stated otherwise. Graphene oxide (GO) powder was purchased from XFNANO Co. Ltd. In a typical experiment, 100 mg of GO powder was dispersed in a 60 mL deionized water with ultrasound for 1 h to form GO dispersion. L-ascorbic acid (LAA, 60 mg), 1.5 mmol of $Ni(NO_3)_2{\cdot}6H_2O$, and 0.5 mmol of $Fe(NO_3)_3{\cdot}9H_2O$ were added to GO dispersion in sequence. The introduction of LAA plays an important role in morphology modification that LAA can be adsorbed on NiFe-LDH seeds to reduce the surface energy for further evolving into ultrathin NiFe-LDH nanosheets.[30] After stirring for 10 min, 10 mmol of urea was added into the above solution and stirred for 1 h. The resultant solution was transferred into a 100 mL Teflon-lined stainless steel autoclave and heated at 120 °C for 24 h. The yellow precipitation was collected by centrifuge and washed with water and ethanol three times. The final sample was obtained after vacuum freeze-drying process to maintain the three-dimensional network of structure, named NiFe-LDH/rGO. Pure NiFe-LDH was synthesized with the same hydrothermal method just without adding GO powder in preparation. Pure rGO was also prepared under the same condition without NiFe-LDH precursors. Compared to the chemical synthesis of NiFe-LDH/rGO, NiFe-LDH + rGO was achieved by physically mixing the as-obtained rGO and NiFe-LDH in a mortar and pestle to get the physically mixed composites. The mass ratio of rGO to NiFe-LDH is 1:3, consistent with the mass ratio in NiFe-LDH/rGO according to the differential scanning calorimetry (DSC) results.

2.2. Material Composition and Structural Characterization. Samples were characterized by a scanning electron microscope (SEM, FEI Sirion) equipped with an energy-dispersive X-ray spectroscopy analysis system and a scanning transmission electron microscope (S/TEM, FEI Tecnai G2 F20). Differential scanning calorimetry (DSC 3+ STAR^e System, Mettler Toledo, Switzerland) was used to analyze the thermal behavior of samples in a flowing nitrogen gas atmosphere. The phase identification of samples was conducted by powder X-ray diffractometer (XRD, Bruker D8 Discover, Germany). Fourier transform infrared spectroscopy (FTIR, Bruker VERTEX 70, Germany) was carried out to record the stretching or bending information of various functional groups. Raman spectra were characterized by a Renishaw InVia Raman microscopy using an Ar^+ laser at 514 nm. The surface chemistry of samples was performed on a Kratos Axis Ultra DLD X-ray photoelectron spectroscopy (XPS).

2.3. Electrochemical Property and Performance Measurements. Active materials (70 wt %), conductive carbon (20 wt %), and polyvinylidene fluoride (10 wt %) were mixed and then dispersed in *N*-methyl-2-pyrrolidone (NMP) to make a homogeneous slurry. The slurry was cast on a copper foil and dried at 80 °C for 5 h, which were then punched into disks with a diameter of 10 mm and dried under vacuum at 120 °C overnight to remove the NMP and water. The electrode disks of different samples were designed to the same thickness of 150 μm, and the corresponding mass loadings of active materials are 1.6 mg cm^{-2} except for rGO with 0.8 mg cm^{-2} due to a much lower bulk density. The half-cell was assembled in an argon-filled glovebox with lithium metal as the counter electrode, Celgard 2400 as the separator, and 1 M lithium hexafluorophosphate ($LiPF_6$) dissolved in a mixed solvent of ethylene carbonate, dimethyl carbonate, and ethyl methyl carbonate (1:1:1, v/v/v) as the electrolyte. The full cell of the lithium-ion capacitor (LIC) was

DOI: 10.1021/acsami.9b10719
ACS Appl. Mater. Interfaces 2019, 11, 35977−35986

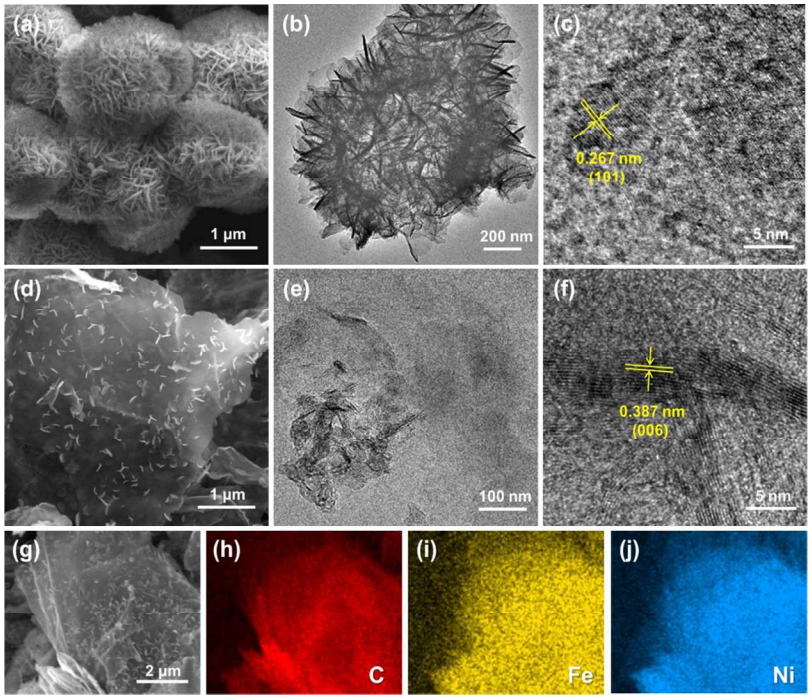

Figure 1. (a) SEM, (b) TEM, and (c) HRTEM images of NiFe-LDH, showing microspheres consisting of aggregated nanosheets. (d) SEM, (e) TEM, and (f) HRTEM images of NiFe-LDH/rGO, with highly dispersed NiFe-LDH nanosheets on rGO. (g–j) Elemental mapping images of NiFe-LDH/rGO, indicating a uniform distribution of C, Ni, and Fe.

fabricated using the NiFe-LDH/rGO as the anode and the mesoporous carbon microspheres (MCMs) as the cathode. MCM was obtained by a facile spray-drying method; more details of MCM fabrication and MCM cathode preparation are shown in our published work.[31] Before assembling LIC, the prelithiations of NiFe-LDH/rGO and MCM were separately performed in half-cells with Li metal as the counter electrode under a galvanostatic charge/discharge (GCD) process at 0.05 A g^{-1}. For the half-cell of NiFe-LDH/rGO, it was discharged to 0.01 V and then charged to 3 V until the third fully discharged state with Li^+ intercalated. For the half-cell of MCM, it was charged to 4.2 V and then discharged to 3 V until the third fully charged state with Li^+ desorpted. Then, these two cells were disassembled, and NiFe-LDH/rGO and MCM electrodes were taken out for assembling the LIC. The different mass ratios of the anode and cathode were studied, with 1:6, 1:12, and 1:23. The galvanostatic charge/discharge (GCD) tests were conducted on a battery test system (LAND CT2001A, China). Cyclic voltammograms (CVs) were recorded on a Solartron electrochemical station (SI 1287), combined with an electrochemical impedance spectroscopy system (EIS, SI 1260) to perform electrochemical impedance spectroscopy from 10^5 to 0.01 Hz. Galvanostatic intermittent titration technique (GITT) was adopted to evaluate the reaction kinetics, with a 10 min charge/discharge process followed by a 10 min interval in circles at a current density of 100 mA g^{-1}. All of the electrochemical measurements were conducted at room temperature. The capacities of LIBs and LICs were calculated based on the active mass of the anode. The energy density and the power density of LICs were calculated based on the total active mass of both the cathode and anode materials.

3. RESULTS AND DISCUSSION

The fabrication process of samples is shown in Scheme 1. Pure NiFe-LDH was prepared based on the one-step hydrothermal method, with homogeneous nucleation and growth to microspherical aggregates of nanosheets as shown in Figure 1a,b. The typical lattice fringes with a distance of 0.267 nm can be clearly observed in the high-resolution TEM (HRTEM) image in Figure 1c, which relates to the (101) facet of NiFe-LDH. NiFe-LDH/rGO was fabricated by introducing negatively charged GO into the NiFe-LDH precursor solution to adsorb positive Ni^{2+} and Fe^{3+} and provide heterogeneous nucleation sites for NiFe-LDH. Figure 1d,e shows the morphology of NiFe-LDH/rGO, exhibiting the uniform NiFe-LDH nanosheets dispersed and anchored on rGO surface, which can be confirmed further by elemental mapping images in Figure 1g–j, favorable to high conductivity and fast ion diffusion during the charge/discharge process. The HRTEM image in Figure 1f demonstrates typical lattice fringes with a distance of 0.387 nm corresponding to (006) facet of NiFe-LDH. Theoretically, a driving force ($\Delta\mu$) is required for the crystal nucleation, which is inversely proportional to the square root of the activation energy (ΔG), as shown in the following equation

$$\Delta\mu = 4V\sqrt{\frac{\pi\alpha^3 f}{3\Delta G}} \quad (1)$$

where V is the solute molar volume, α is the surface energy between the liquid and solid interfaces, and f is the wetting angle factor, for homogeneous nucleation $f = 1$, for heterogeneous nucleation $f < 1$.[32,33] Accordingly, less activation energy is required for heterogeneous nucleation than for homogeneous nucleation. The introduction of rGO produces the solid/liquid interface to induce the highly dispersed heterogeneous nucleation of NiFe-LDH on rGO surface instead of homogeneous self-nucleation, beneficial to avoid nanostructure aggregation. For better illustrating the impacts of chemical bonding LDH to rGO, NiFe-LDH + rGO was prepared by physically mixing as-obtained NiFe-LDH and rGO in a mortar and pestle. Figure S1a displays the morphology of NiFe-LDH + rGO, with no evident combination with rGO. Pure rGO was also prepared without

DOI: 10.1021/acsami.9b10719
ACS Appl. Mater. Interfaces 2019, 11, 35977–35986

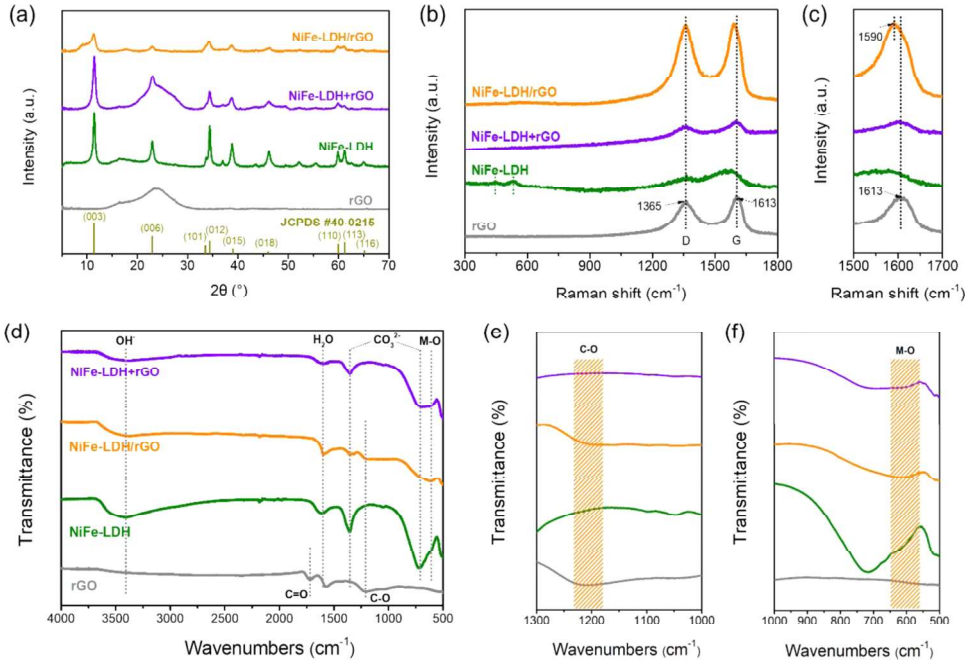

Figure 2. (a) XRD pattern, (b) Raman spectra, (c) magnified G-band in Raman spectra, (d) FTIR spectra, (e) C–O vibration, and (f) M–O (M = Ni, Fe) vibration in FTIR spectra of samples.

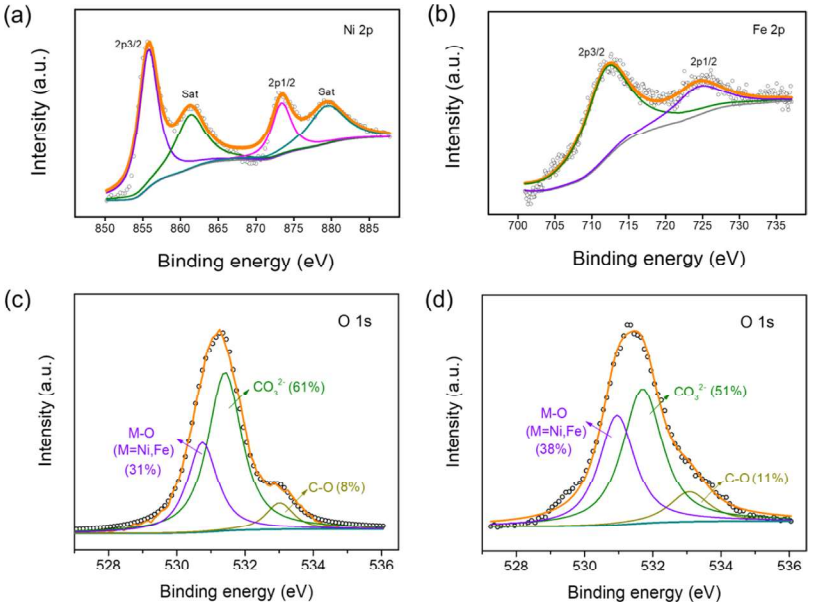

Figure 3. (a) Ni 2p and (b) Fe 2p XPS spectra of NiFe-LDH/rGO. O 1s XPS spectra of (c) NiFe-LDH + rGO and (d) NiFe-LDH/rGO.

adding LDH, a two-dimensional sheet structure shown in Figure S1b.

Figure 2a shows XRD patterns; diffraction peaks of NiFe-LDH are indexed to $Ni_{0.75}Fe_{0.25}$ $(CO_3)_{0.125}(OH)_2{\cdot}0.38H_2O$ (JCPDS #40-0215). NiFe-LDH + rGO shows the same XRD pattern as NiFe-LDH and a diffraction hump between 20 and 28°, ascribed to rGO in composites, just like the XRD pattern of pure rGO sample. NiFe-LDH/rGO shows no diffraction hump. Although it is not known what exactly happened, the disappearance of this diffraction peak likely suggests the change of surface or interface between rGO and LDH grown on it. A little peak at about 9° is shown, near to the peak assigning to (003) plane. It is not able to index the peak, though it might be ascribed to the fact that the introduction of negatively charged GO during the preparation induces a partially broadened interlayer spacing of NiFe-LDH, leading to a peak appearing at a smaller angle than that of (003) plane.[34] The crystallite size of samples was calculated using the Scherer equation based on the XRD patterns, different from the particle size or nanosheet size. NiFe-LDH/rGO exhibits small crystallites of 5.5 nm compared to NiFe-LDH of 15.1 nm, likely due to the introduction of rGO in material preparation, which efficiently provides heterogeneous nucleation sites for high nucleation density for NiFe-LDH and simultaneously restrains the continuous growth of crystals. DSC results in Figure S2 demonstrate the weight change and heat flow with the increase

DOI: 10.1021/acsami.9b10719
ACS Appl. Mater. Interfaces 2019, 11, 35977–35986

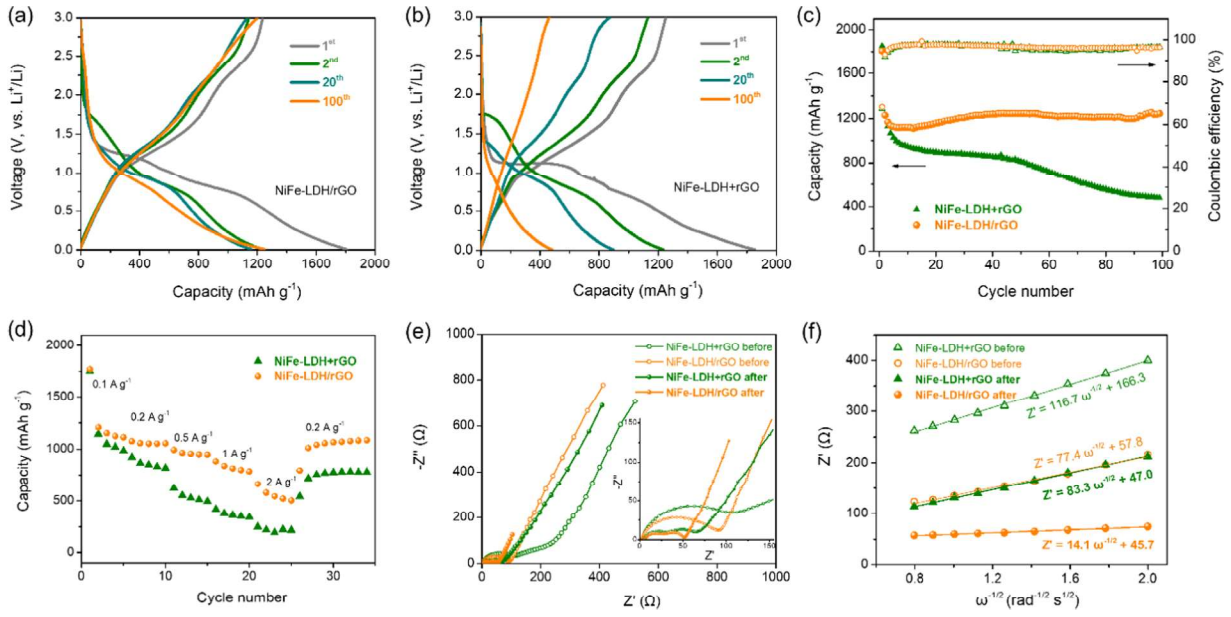

Figure 4. GCD profiles of (a) NiFe-LDH/rGO and (b) NiFe-LDH + rGO at the current density of 100 mA g^{-1}. (c) Cycling performance of samples at a current density of 100 mA g^{-1}. (d) Rate capacity of samples. The capacity was calculated based on the active mass of the anode. (e) Nyquist plots of samples at the pristine state and after cycling. The inset in part e is the magnified Nyquist plot. (f) Relationship between the real part of impedance and low frequencies; the smaller the slopes of the fitting curve, the faster ion diffusion during the charge/discharge process.

of temperature. Pure NiFe-LDH illustrates two weight-loss plateaus corresponding to the loss of physical and crystalline water, and the removal of hydroxyl and carbonate groups, respectively. Heat flow curve shows the same phenomenon indicating two endothermic processes that occurred during temperature increase. Beyond that, NiFe-LDH/rGO still exhibits the third plateaus with a 25 wt % weight loss, attributed to the rGO combustion showing an exothermic peak in heat flow curve. Therefore, the mass ratio of rGO and NiFe-LDH in NiFe-LDH/rGO is 1:3. Physically mixed NiFe-LDH + rGO was prepared based on this mass ratio. Raman spectra are shown in Figure 2b,c. NiFe-LDH performs a low Raman activity with weak peaks at fingerprint regions of about 447 and 533 cm^{-1}, which are difficult to be identified in NiFe-LDH/rGO and NiFe-LDH + rGO after the introduction of rGO. The peaks at 1365 and 1580 cm^{-1} originate from the disordered structure (D-band) and the C−C stretch (G-band) with sp^2 carbon structure in NiFe-LDH. Comparing three samples containing rGO, the D-band locates at the same position of 1365 cm^{-1}, but the G-band shifts from 1613 to 1590 cm^{-1} for NiFe-LDH/rGO, which can be clearly observed in Figure 2c. It illustrates a charge-transfer process from rGO to NiFe-LDH in NiFe-LDH/rGO.[35] Physically mixed NiFe-LDH + rGO shows no G-band shift due to the weak electrostatic interaction between rGO and NiFe-LDH. NiFe-LDH/rGO demonstrates a little higher relative intensity of D-band than other samples, ascribed to the fact that the formation of chemical bonds between rGO and NiFe-LDH creates new defects. Figure 2d displays the FTIR spectra; the absorption peaks at 3406 and 1597 cm^{-1} represent the stretching vibration of O−H and water molecules, respectively.[36] The stretching and bending vibrations of CO_3^{2-} display at the peaks of 1354 and 715 cm^{-1}.[37] All of these four peaks can be observed in the FTIR spectra of NiFe-LDH/rGO, NiFe-LDH + rGO, and NiFe-LDH. For rGO, the vibrations of C═O at 1718 cm^{-1} and C−O at 1207 cm^{-1} are distinguishable, which is indistinguishable in NiFe-LDH + rGO. NiFe-LDH/rGO exhibits a similar phenomenon, but a little peak of C−O vibration can be seen in the magnified spectra in Figure 2e. NiFe-LDH/rGO also shows a little stronger vibration peak of M−O (M = Ni, Fe) in Figure 2f. These enhancements are ascribed to the oxygen bridges between NiFe-LDH and rGO, originating from chemical connections between oxygen-containing groups on rGO and NiFe-LDH during preparation.

Figure 3 shows the high-resolution XPS spectra of samples; the survey XPS spectra can be seen in Figure S3a, with distinguishable peaks of elements C, O, Ni, and Fe for both NiFe-LDH + rGO and NiFe-LDH/rGO. For NiFe-LDH/rGO, Ni 2p spectra in Figure 3a exhibit two main peaks at 855.6 eV and 873.3 eV assigned to Ni $2p_{3/2}$ and Ni $2p_{1/2}$ with a valence state of +2, accompanied by two satellite peaks at 862.2 and 879.0 eV, respectively. Fe 2p spectra in Figure 3b show two peaks located at 712.6 and 725.5 eV, which correspond to Fe $2p_{3/2}$ and Fe $2p_{1/2}$ with a valence state of +3. Figure S3b performs Ni 2p and Fe 2p spectra of NiFe-LDH + rGO, with Ni^{2+} and Fe^{3+} in materials. For O 1s XPS spectra, NiFe-LDH + rGO (Figure 3c) and NiFe-LDH/rGO (Figure 3d) are decomposed into three peaks, relating to M−O, CO_3^{2-}, and C−O, respectively. Theoretically, the intensity of M−O bond and C−O bond originated from NiFe-LDH in NiFe-LDH + rGO and NiFe-LDH/rGO should be the same. The enhanced signals of M−O bond and C−O bond for NiFe-LDH/rGO in Figure 3d should be ascribed to chemical connections in the interface between NiFe-LDH and rGO bonded during the chemically synthetic process, which cannot be observed in NiFe-LDH + rGO. It is also consistent with Raman and FTIR results in Figure 2. And NiFe-LDH/rGO demonstrates a little peak shift to higher binding energy compared to NiFe-LDH + rGO, with M−O bond from 530.75 to 530.95 eV, CO_3^{2-} from 531.35 to 531.45 eV, and C−O bond from 533.05 to 533.15 eV, indicating the enhanced strength of chemical bonds after the chemical introduction of rGO.

DOI: 10.1021/acsami.9b10719
ACS Appl. Mater. Interfaces 2019, 11, 35977−35986

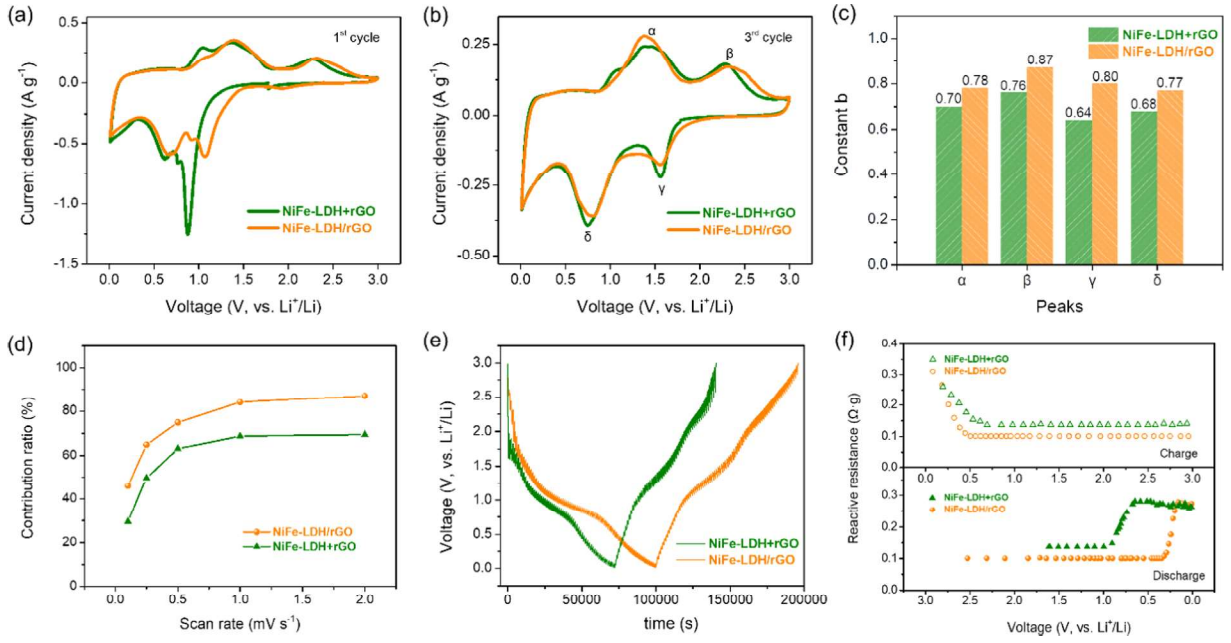

Figure 5. CV curves of samples of (a) first cycle and (b) third cycle at the scan rate of 0.1 mV s^{-1}. (c) *b* values of samples at different redox peaks, calculated based on multirate CV results. (d) Capacitive contribution of samples at different scan rates. (e) GITT plot of samples tested at 100 mA g^{-1} and (f) the corresponding reactive resistances (RR) during the charge/discharge process.

The electrochemical properties of samples were characterized by means of galvanostatic charge/discharge (GCD) cycling with the results shown in Figure 4a,b. Figure 4a displays the GCD profiles at different cycles at 100 mA g^{-1} of NiFe-LDH/rGO, possessing several charge/discharge plateaus with multistep delithiation/lithiation processes, and most discharge capacity is at a voltage window of 0.01–1.25 V. For the first cycle, NiFe-LDH/rGO exhibits a discharge capacity of 1806 mAh g^{-1}, evidently higher than the charge capacity of 1236 mAh g^{-1}, with the initial coulombic efficiency of 68.4%, which is ascribed to the solid electrolyte interface (SEI) layer formation and irreversible Li^+ consume for side reactions in the electrolyte.[38,39] After that, NiFe-LDH/rGO retains a stable capacity. In Figure 4b, NiFe-LDH + rGO demonstrates the same initial coulombic efficiency as NiFe-LDH/rGO but displays the fast capacity fading after the 20th cycle due to the unstable structure with a weak interaction between rGO and NiFe-LDH. GCD profiles of pure rGO and NiFe-LDH are shown in Figure S4. NiFe-LDH exhibits more severe irreversibility than NiFe-LDH + rGO, while rGO shows great capacity retention without being limited by ion diffusion. The redox reactions and electrochemical mechanism are further discussed below in CV curves. Figure 4c shows the corresponding cycling performance of samples at 100 mA g^{-1}. NiFe-LDH/rGO illustrates the excellent cycling stability in the organic electrolyte, maintaining 1202 mAh g^{-1} of discharge capacity after 100 cycles, absolutely higher than 463 mAh g^{-1} of NiFe-LDH + rGO, also superior to 512 mAh g^{-1} of rGO (Figure S5a) and 463 mAh g^{-1} of NiFe-LDH (Figure S5b). The capacity decay of NiFe-LDH + rGO during cycling especially after 50 cycles could be ascribed to the fact that severe aggregation impedes the efficient ion diffusion. Rate performance of samples was also assessed as shown in Figure 4d and tested at various current densities from 0.1 to 2 A g^{-1}. NiFe-LDH/rGO and NiFe-LDH + rGO demonstrate the similar initial capacities of 1771 and 1750 mAh g^{-1}, respectively, a little lower than 1958 mAh g^{-1} of NiFe-LDH (Figure S5d) due to the introduction of lower-capacity rGO of 1524 mAh g^{-1} (Figure S5c). With the increase of current density, NiFe-LDH/rGO exhibits the advantage of excellent rate performance, with 1151, 1054, 957, 816, and 543 mAh g^{-1} at 0.1, 0.2, 0.5, 1, and 2 A g^{-1}, respectively, better than NiFe-LDH + rGO, NiFe-LDH, and rGO. It is superior to the reported NiCo-LDH/eRG with 1075 mAh g^{-1} at 0.1 A g^{-1} and 257 mAh g^{-1} at 3 A g^{-1},[2121] and published NiFe-LDH/rGO with 959 mAh g^{-1} at 0.1 A g^{-1} and 407 mAh g^{-1} at 0.8 A g^{-1}.[1818] Followed by a reduction of current density to 0.2 A g^{-1}, the capacity of NiFe-LDH/rGO still restores to 1041 mAh g^{-1}. A more detailed comparison of the electrochemical performance of our work and the reported LDH and derived layered double oxide (LDO) in LIBs is summarized in Table S1. Compared to pure NiFe-LDH, NiFe-LDH + rGO shows a little performance enhancement probably originated from higher electrical conductivity after mixing rGO with NiFe-LDH. The more excellent rate performance of NiFe-LDH/rGO compared to that of NiFe-LDH + rGO should not be partially attributed to the conductivity improvement; the following plays a more important role: (1) chemical introduction of rGO induces the heterogeneous nucleation of NiFe-LDH on rGO, establishes the chemical-bonded interaction between rGO and NiFe-LDH, and accelerates the charge transfer during charge/discharge process; (2) rGO sheets restrain the crystal growth of NiFe-LDH with a smaller crystallite size and facilitate the highly dispersed nanosheet structure formation, conducive to fast ion diffusion, especially at high rates; and (3) NiFe-LDH effectively prevents the rGO from aggregating and restacking. EIS spectra are shown in Figure 4e. At the pristine state, NiFe-LDH/rGO demonstrates a semicircle at high frequencies corresponding to the charge-transfer resistance of 88.8 Ω, lower than that of rGO and NiFe-LDH (Figure S6a,b), attributable to chemical bonding NiFe-LDH on rGO and thus an integral structure with an interface for effective charge transfer. NiFe-LDH + rGO at the pristine state exhibits a semicircle and a quasi-linear part at high

DOI: 10.1021/acsami.9b10719
ACS Appl. Mater. Interfaces 2019, 11, 35977–35986

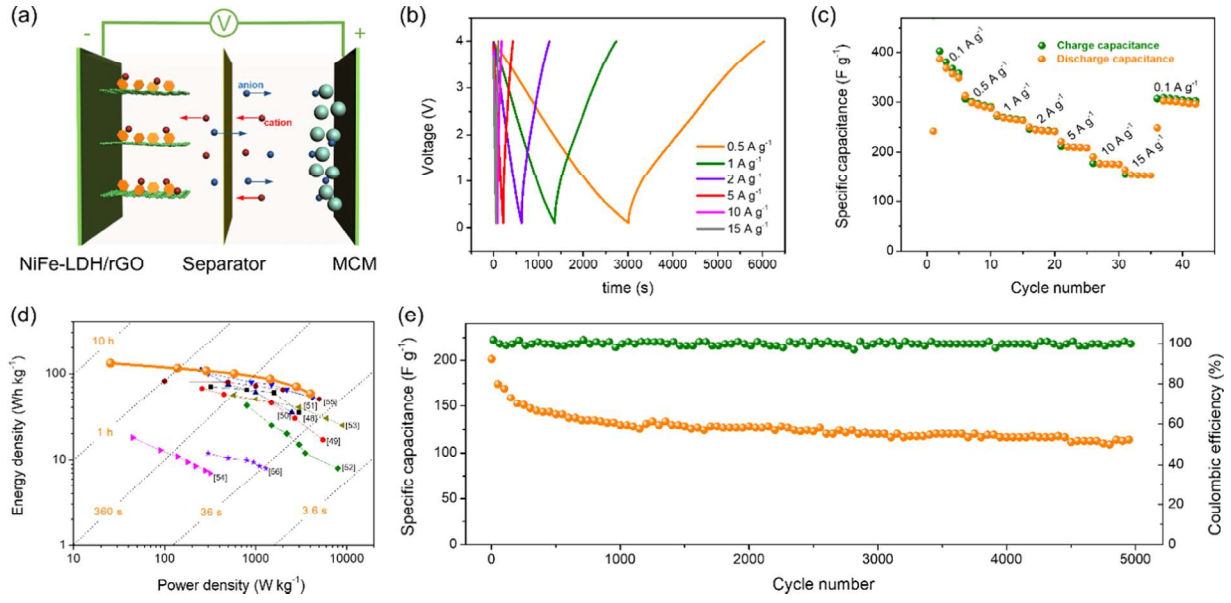

Figure 6. (a) Schematic illustration of NiFe-LDH/rGO//MCM capacitor. (b) GCD profiles and (c) the corresponding rate performance of the full capacitor at various current densities, calculated based on the active mass of the anode. (d) Ragone plot of the full capacitor, calculated based on the total active mass of the cathode and anode. (e) Cycling performance of the full capacitor at a current density of 5 A g^{-1}.

frequencies, with a charge-transfer resistance of 105.9 Ω. It could be ascribed to the less well-connected interface in physically mixed NiFe-LDH + rGO. After cycling, both NiFe-LDH/rGO and NiFe-LDH + rGO display two semicircles at high frequencies, which correspond to the SEI layer and internal material structure. For NiFe-LDH + rGO, NiFe-LDH and rGO aggregate during a charge/discharge process, which leads to one interface disappearing and thus retains two interfaces after cycling. NiFe-LDH/rGO still possesses the advantage of lower resistance due to the unique nanostructure. An inclining line at low frequencies demonstrates the ion diffusion process.[40] Figure 4f plots the relationship between the real part of impedance and frequencies, from which the Li^+ diffusion coefficients (D_{Li}^+, details shown in Supporting Information) were calculated. At the pristine state, NiFe-LDH/rGO exhibits a high D_{Li}^+ of 3.74×10^{-13} cm^2 s^{-1}, twice that of NiFe-LDH + rGO of 1.64×10^{-13} cm^2 s^{-1}, also superior to rGO and NiFe-LDH (Figure S6c,d). After cycling with the formation of a stable SEI, NiFe-LDH/rGO performs an enhanced ion diffusion ability with a D_{Li}^+ of 1.13×10^{-12} cm^2 s^{-1}, still higher than NiFe-LDH + rGO of 3.22×10^{-13} cm^2 s^{-1}, showing the great potential for fast ion diffusion even after many charge/discharge cycles.

Figure 5a,b shows CV curves tested from 0.01 to 3.0 V versus Li^+/Li at a scan rate of 0.1 mV s^{-1}. Figure 5a compares the CV curves of the first cycle of NiFe-LDH/rGO and NiFe-LDH + rGO. In the first cathodic scan for NiFe-LDH/rGO, two peaks appear at 1.07 and 0.67 V, relating to the electrolyte decomposition to form SEI layer and conversion of Ni^{2+} to Ni^0 and Fe^{3+} to $Fe^{0.}$[18] The corresponding peaks for NiFe-LDH + rGO locate at the lower voltages of 0.88 and 0.62 V, impeded by interfacial kinetics (Figure 4e). In the first anodic scan, NiFe-LDH/rGO shows a peak at a voltage of 2.31 V, and a composite peak consisting of a weak peak at 1.06 V and a distinguishable peak at 1.39 V, ascribed to the oxidation of Ni^0 to Ni^{2+}, consistent with the redox behavior of $Ni(OH)_2$ in literatures.[18] The composite peak illustrates the one-step fast reactions with an indistinguishable peak of the first redox reaction. The oxidation of Fe^0 to Fe^{3+} occurs at about 1.39 V, just like that for reported Fe_2O_3.[18] For NiFe-LDH + rGO and NiFe-LDH (Figure S7a), the peak at 1.06 V in the anodic scan is more distinguishable, which illustrates two-step redox reactions separately occurring at 1.06 and 1.39 V. For rGO in Figure S7b, it displays the capacity by Li^+ combination on surface defects without redox reactions showing no evident peaks in CV curves. In the third cycle in Figure 5b, NiFe-LDH/rGO and NiFe-LDH + rGO perform similar CV curves. The peak located at 1.07 V shifts near to 1.6 V in the cathodic scan, illustrating the activation of electrodes.[41] The anodic scan is coincident with that in the first cycle. And both of them show the same shape as the second cycle (Figure S7c,d). EIS spectra after the first three cycles were tested and are shown in Figure S8. NiFe-LDH/rGO and NiFe-LDH + rGO exhibit similar resistance, which is in agreement with the similar CV curves in Figure 5b. It could indicate that the structure superiority of NiFe-LDH/rGO is not prominent at first several charge/discharge cycles but distinguishes after long cycles (Figure 4e). The CV curves of samples at different scan rates are recorded in Figure S9 for identifying whether the electrochemical behavior is surface-controlled or diffusion-controlled and for calculating the corresponding contributions. The response current and the scan rate conform to the following relationship[42,43]

$$i = a\nu^b \tag{2}$$

where a and b are adjustable parameters. The b value is an index for distinguishing the electrochemical behavior; b equals 0.5 and 1 for the diffusion-controlled and the surface-controlled processes, respectively.[44] Figure 5c shows the b values of samples at different oxidation/reduction states, with the value between 0.5 and 1, indicative of the combined diffusion–surface-controlled process for all samples. NiFe-LDH/rGO shows higher values compared to NiFe-LDH + rGO although they contain the same amount of rGO, which originates from the great interfacial interaction and unique nanostructure for effective charge transfer and fast ion

DOI: 10.1021/acsami.9b10719
ACS Appl. Mater. Interfaces 2019, 11, 35977−35986

diffusion. The relationship of the response current and the scan rate can also be expressed as follows[45,46]

$$i = k_1\nu + k_2\nu^{1/2} \quad (3)$$

where $k_1\nu$ is the surface-controlled part and $k_2\nu^{1/2}$ is the diffusion-controlled part. The calculated contribution results are performed in Figures 5d and S10. Compared to NiFe-LDH in Figure S10a, both NiFe-LDH/rGO and NiFe-LDH + rGO in Figure 5d demonstrate a higher capacitive contribution after introducing the rGO into materials. Interestingly, a 15% contribution gap still exists between NiFe-LDH/rGO and NiFe-LDH + rGO at all scan rates, which is attributed to the unique chemical effect of rGO on the morphology modification of NiFe-LDH nanosheets and interface optimization between rGO and NiFe-LDH. For pure rGO in Figure S10b, it displays a high capacitive contribution, especially at high scan rates, not limited by ion diffusion for redox reactions. GITT is used to record the relaxation behavior of voltage after the intermittent charge/discharge process, an indication of ion diffusion ability at a different charge/discharge state. The reactive resistance (RR) is a quantified factor for the comparison of reaction kinetics, calculated based on IR drop and the current density.[47] Figure 5e shows the GITT plots of samples at a current density of 100 mA g^{-1}. NiFe-LDH/rGO exhibits a longer charge/discharge time with a higher capacity than NiFe-LDH + rGO. The corresponding RR is calculated as shown in Figure 5f. NiFe-LDH/rGO performs a lower RR compared to NiFe-LDH + rGO during both charge and discharge processes, illustrating an enhancement of reaction kinetics.

Lithium-ion capacitors were assembled with NiFe-LDH/rGO as the anode and mesoporous carbon microspheres (MCMs) as the cathode, and the schematic illustration is shown in Figure 6a. MCM was prepared based on an efficient spray-drying method.[31] MCM possesses excellent spherical morphology (Figure S11a) and uniform mesoporous structure (Figure S11b,c) with an average pore size of 9.5 nm (Figure S11d), a large surface area of 1282 m^2 g^{-1}, and a high pore volume of 2.90 m^3 g^{-1}, beneficial to fast ion diffusion, and is expected to be a promising candidate as cathode for LICs. The electrochemical performance of the MCM cathode in the half-cell with the Li metal anode was tested, with 81 F g^{-1} at 0.1 A g^{-1} and 23 F g^{-1} at 2 A g^{-1} (Figure S12), showing a great electrochemical activity. For fabricating LIC, NiFe-LDH/rGO and MCM are separately prelithiated for three cycles in half-cells with Li metal as a counter electrode, which provides sufficient Li^+ sources for irreversible Li^+ consume for SEI layer formation and side reactions in the electrolyte, especially at the first cycle. The GCD profiles of prelithiated process are shown in Figure S13. Then, the LIC is assembled by the fully discharged NiFe-LDH/rGO with Li^+ intercalated and the fully charged MCM with Li^+ desorbed. The rate performance (Figure S14a) and Ragone plots (Figure S14b) are compared based on the different mass ratio of NiFe-LDH/rGO anode to MCM cathode, with 1:6, 1:12, and 1:23. The mass increase of MCM leads to a specific capacitance enhancement but sacrifices the energy density and power density of LIC, which needs a trade-off between them. Considering the practical requirements for LIC, the mass ratio of 1:6 is chosen for further tests in our work. The GCD profiles of NiFe-LDH/rGO//MCM are shown in Figure 6b with a voltage window of 0.1–4.0 V. NiFe-LDH/rGO//MCM is first discharged to achieve Li^+ deintercalation from the anode and adsorption on the cathode. The opposite process occurred when charged. GCD profiles demonstrate the near-linear shape with no evident IR drop even at high current densities, indicative of a great reversibility of charge/discharge process with low resistance. Figure 6c displays the corresponding specific capacitance of NiFe-LDH/rGO//MCM at various current densities. NiFe-LDH/rGO//MCM shows a high capacitance of 367 F g^{-1} at 0.1 A g^{-1} and maintains 153 F g^{-1} at 15 A g^{-1}. The great rate performance stems from two aspects: (1) NiFe-LDH/rGO possesses a highly dispersed layered structure with good conductive rGO as the substrate, providing adequate active sites for sufficient Li^+ intercalation even at high rates; (2) the dominant mesoporous structure of MCM is desirable for fast ion diffusion in both aqueous and organic electrolyte systems. Ragone plot in Figure 6d reflects the relationship between the energy density and the power density. NiFe-LDH/rGO//MCM delivers an ultrahigh energy density of 133 Wh kg^{-1} at 26 W kg^{-1} and a power density of 4016 W kg^{-1} at 58 Wh kg^{-1}, comparable to the reported results,[48−56] summarized in Table S2. Figure 6e shows the cycling performance of NiFe-LDH/rGO//MCM at 5 A g^{-1}. It exhibits a capacitance decrease initially but sustains stable for 5000 cycles with great cycling stability. Above all, NiFe-LDH/rGO//MCM combines the advantages of batteries with high energy density and supercapacitors with long cycling stability and high power density, offering good opportunities to meet the needs for cost-effective and high-efficiency energy storage systems.

4. CONCLUSIONS

NiFe-LDH/rGO with dispersed NiFe-LDH nanosheets chemically bonded on rGO is fabricated by a one-step hydrothermal process and demonstrates excellent electrochemical properties as an anode material for LIBs and LICs. The unique structure of NiFe-LDH/rGO composites offers synergistic effects with (1) great dispersion of NiFe-LDH nanosheets with increased accessible active sites, (2) reduced crystallite size for fast ion diffusion and high-rate charge/discharge performance, (3) high conductivity to improve the electron transfer, and (4) chemical modification of the surface chemistry of rGO. Benefiting from these advantages, NiFe-LDH/rGO in LIBs exhibits a higher rate performance (1151 mAh g^{-1} at 100 mA g^{-1}, 543 mAh g^{-1} at 2000 mA g^{-1}) and a better cycling stability (1202 mAh g^{-1} after 100 cycles at 100 mA g^{-1}) than both NiFe-LDH and physically mixed NiFe-LDH + rGO. The corresponding LIC with NiFe-LDH/rGO anode and MCM cathode demonstrates high energy density and high power density simultaneously, with 133 Wh kg^{-1} at 25 W kg^{-1} and 4016 W kg^{-1} at 58 Wh kg^{-1}, providing a promising candidate for the next-generation high-efficiency hybrid energy storage systems.

■ ASSOCIATED CONTENT

Supporting Information

The Supporting Information is available free of charge on the ACS Publications website at DOI: 10.1021/acsami.9b10719.

SEM images, DSC results, survey XPS spectra of samples, GCD profiles, cycling performance, Nyquist plots, CV curves of the first three cycles, capacitive contributions at various scan rates, rate performance of MCM cathode, comparison of electrochemical performance of LDH and LDO in LIBs, and comparison of energy density and power density (PDF)

DOI: 10.1021/acsami.9b10719
ACS Appl. Mater. Interfaces 2019, 11, 35977−35986

AUTHOR INFORMATION

Corresponding Authors

*E-mail: longdh@mail.ecust.edu.cn (D.L.).
*E-mail: gzcao@uw.edu (G.C.).

ORCID

Donghui Long: 0000-0002-3179-4822
Guozhong Cao: 0000-0001-6539-0490

Notes

The authors declare no competing financial interest.

ACKNOWLEDGMENTS

This work was supported by the National Science Foundation (CBET-1803256), the National Science Foundation of China (No. 21576090), and the Fundamental Research Funds for the Central Universities (222201718002). Part of this work was conducted at the Molecular Analysis Facility, a National Nanotechnology Coordinated Infrastructure site at the University of Washington, which is supported, in part, by the National Science Foundation (grant NNCI-1542101), the University of Washington, the Molecular Engineering & Sciences Institute, and the Clean Energy Institute. M.T. and J.Z. acknowledge the financial support from CSC for this work at the University of Washington.

REFERENCES

(1) Naoi, K.; Ishimoto, S.; Miyamoto, J.; Naoi, W. Second Generation 'Nanohybrid Supercapacitor': Evolution of Capacitive Energy Storage Devices. *Energy Environ. Sci.* **2012**, *5*, 9363−9373.

(2) Aravindan, V.; Gnanaraj, J.; Lee, Y.; Madhavi, S. Insertion-Type Electrodes for Nonaqueous Li-Ion Capacitors. *Chem. Rev.* **2014**, *114*, 11619−11635.

(3) Wang, H.; Zhu, C.; Chao, D.; Yan, Q.; Fan, H. J. Nonaqueous Hybrid Lithium-Ion and Sodium-Ion Capacitors. *Adv. Mater.* **2017**, *1702093*, 1−18.

(4) Fu, S.; Yu, Q.; Liu, Z.; Hu, P.; Chen, Q.; Feng, S.; Mai, L.; Zhou, L. Yolk-Shell Nb_2O_5 Microspheres as Intercalation Pseudocapacitive Anode Materials for High-Energy Li-Ion Capacitors. *J. Mater. Chem. A* **2019**, *7*, 11234−11240.

(5) Liu, C.; Ren, Q.; Zhang, S.; Yin, B.; Que, L.; Zhao, L.; Sui, X. High Energy and Power Lithium-Ion Capacitors Based on Mn_3O_4/3D-Graphene as Anode and Activated Polyaniline-Derived Carbon Nanorods as Cathode. *Chem. Eng. J.* **2019**, *370*, 1485−1492.

(6) Park, M.; Lim, Y.; Kim, J.; Kim, Y.; Cho, J.; Kim, J. A Novel Lithium-Doping Approach for an Advanced Lithium Ion Capacitor. *Adv. Energy Mater.* **2011**, *1*, 1002−1006.

(7) Du, H.; Yang, H.; Huang, C.; He, J.; Liu, H.; Li, Y. Graphdiyne Applied for Lithium-Ion Capacitors Displaying High Power and Energy Densities. *Nano Energy* **2016**, *22*, 615−622.

(8) Liu, C.; Zhang, C.; Song, H.; Zhang, C.; Liu, Y.; Nan, X.; Cao, G. Mesocrystal MnO Cubes as Anode for Li-Ion Capacitors. *Nano Energy* **2016**, *22*, 290−300.

(9) Wang, H.; Guan, C.; Wang, X.; Fan, H. J. A High Energy and Power Li-Ion Capacitor Based on A TiO_2 Nanobelt Array Anode and A Graphene Hydrogel Cathode. *Small* **2015**, *11*, 1470−1477.

(10) Luo, J.; Zhang, W.; Yuan, H.; Jin, C.; Zhang, L.; Huang, H.; Liang, C.; et al. Pillared Structure Design of MXene with Ultralarge Interlayer Spacing for High-Performance Lithium-Ion Capacitors. *ACS Nano* **2017**, *11*, 2459−2469.

(11) Wang, Z.; Zhou, L.; Lou, X. W. Metal Oxide Hollow Nanostructures for Lithium-Ion Batteries. *Adv. Mater.* **2012**, *24*, 1903−1911.

(12) Wu, H.; Chan, G.; Choi, J. W.; Ryu, I.; Yao, Y.; Mcdowell, M. T.; Lee, S. W.; Jackson, A.; Yang, Y.; Hu, L.; Cui, Y. Stable Cycling of Double-Walled Silicon Nanotube Battery Anodes through Solid−Electrolyte Interphase Control. *Nat. Nanotechnol.* **2012**, *7*, 310−315.

(13) Wu, R. S.; Ren, W.; Xu, L.; Cheng, H. M. Doped Graphene Sheets As Anode Materials with Superhigh Rate and Large Capacity for Lithium Ion. *ACS Nano* **2011**, *5*, 5463−5471.

(14) Wang, T.; Wu, J.; Liu, Y.; Cui, X.; Ding, P.; Deng, J.; Zha, C.; Coy, E.; Li, Y. Scalable Preparation and Stabilization of Atomic-Thick CoNi Layered Double Hydroxide Nanosheets for Bifunctional Oxygen Electrocatalysis and Rechargeable Zinc-Air Batteries. *Energy Storage Mater.* **2019**, *16*, 24−30.

(15) Liu, Y.; Yu, X.; Fang, Y.; Zhou, X.; Bao, J.; Zhou, X.; Lou, X. W. Confining SnS_2 Ultrathin Nanosheets in Hollow Carbon Nanostructures for Efficient Capacitive Sodium Storage Confining SnS_2 Ultrathin Nanosheets in Hollow Carbon Nanostructures for Efficient Capacitive Sodium Storage. *Joule* **2018**, *2*, 725−735.

(16) Zhou, J.; Qin, J.; Zhang, X.; Shi, C.; Liu, E.; Li, J.; Zhao, N.; He, C. 2D Space-Confined Synthesis of Few-Layer MoS_2 Anchored on Carbon Nanosheet for Lithium-Ion Battery Anode. *ACS Nano* **2015**, *9*, 3837−3848.

(17) Zhang, J.; Xiao, K.; Zhang, T.; Qian, G.; Wang, Y.; Feng, Y. Porous Nickel-Cobalt Layered Double Hydroxide Nanoflake Array Derived from ZIF-L-Co Nanoflake Array for Battery-Type Electrodes with Enhanced Energy Storage Performance. *Electrochim. Acta* **2017**, *226*, 113−120.

(18) Zhang, M.; Wei, Z.; Wang, T.; Muhammad, S.; Zhou, J.; Liu, J.; Zhu, J.; Hu, J. Nickel-Iron Layered Double Hydroxides and Reduced Graphene Oxide Composite with Robust Lithium Ion Adsorption Ability for High-Capacity Energy Storage Systems. *Electrochim. Acta* **2019**, *296*, 190−197.

(19) Zhang, J.; Li, Z.; Chen, Y.; Gao, S.; Wen, X.; Lou, X. W. Nickel−Iron Layered Double Hydroxide Hollow Polyhedrons as A Superior Sulfur Host for Lithium−Sulfur Batteries. *Angew. Chem., Int. Ed.* **2018**, *57*, 10944−10948.

(20) Li, X.; Wu, H.; Guan, C.; Elshahawy, A. M.; Dong, Y.; Pennycook, S. J.; Wang, J. $(Ni,Co)Se_2$/NiCo-LDH Core/Shell Structural Electrode with the Cactus-Like $(Ni,Co)Se_2$ Core for Asymmetric Supercapacitors. *Small* **2019**, *15*, No. 1803895.

(21) Shi, J.; Du, N.; Zheng, W.; Li, X.; Dai, Y.; He, G. Ultrathin Ni-Co Double Hydroxide Nanosheets with Conformal Graphene Coating for Highly Active Oxygen Evolution Reaction and Lithium Ion Battery Anode Materials. *Chem. Eng. J.* **2017**, *327*, 9−17.

(22) Shao, M.; Ning, F.; Zhao, J.; Wei, M.; Evans, D. G.; Duan, X. Preparation of Fe_3O_4@SiO_2@Layered Double Hydroxide Core−Shell Microspheres for Magnetic Separation of Proteins. *J. Am. Chem. Soc.* **2012**, *134*, 1071−1077.

(23) Tonda, S.; Jo, W. Plasmonic Ag Nanoparticles Decorated NiAl-Layered Double Hydroxide/Graphitic Carbon Nitride Nanocomposites for Efficient Visible-Light-Driven Photocatalytic Removal of Aqueous Organic Pollutants. *Catal. Today* **2018**, *315*, 213−222.

(24) Yang, J.; Yu, C.; Fan, X.; Liang, S.; Li, S.; Huang, H.; Ling, Z.; Hao, C.; Qiu, J. Electroactive Edge Site-Enriched Nickel−Cobalt Sulfide into Graphene Frameworks for High-Performance Asymmetric Supercapacitors. *Energy Environ. Sci.* **2016**, *9*, 1299−1307.

(25) Zhou, X.; Wan, L. J.; Guo, Y. G. Synthesis of MoS_2 Nanosheet−Graphene Nanosheet Hybrid Materials for Stable Lithium Storage. *Chem. Commun.* **2013**, *49*, 1838−1840.

(26) Lonkar, S. P.; Raquez, J. M.; Dubois, P. One-Pot Microwave-Assisted Synthesis of Graphene/Layered Double Hydroxide (LDH) Nanohybrids. *Nano-Micro Lett.* **2015**, *7*, 332−340.

(27) Etacheri, V.; Yourey, J. E.; Bartlett, B. M. Chemically Bonded TiO_2 Å Bronze Nanosheet/Reduced Graphene Oxide Hybrid for High-Power Lithium Ion Batteries. *ACS Nano* **2014**, *8*, 1491−1499.

(28) Zhou, G.; Wang, D.; Yin, L.; Li, N.; Li, F.; Cheng, H. Oxygen Bridges between NiO Nanosheets and Graphene for Improvement of Lithium Storage. *ACS Nano* **2012**, *6*, 3214−3223.

(29) Jiang, Y.; Song, Y.; Li, Y.; Tian, W.; Pan, Z.; Yang, P.; Li, Y.; Gu, Q.; Hu, L. Charge Transfer in Ultrafine LDH Nanosheets/Graphene Interface with Superior Capacitive Energy Storage Performance. *ACS Appl. Mater. Interfaces* **2017**, *9*, 37645−37654.

(30) He, J.; Xiong, D.; Wu, J.; Li, Q.; Dravid, V.; Zhao, Y.; et al. Nickel Cobalt Hydroxide @Reduced Graphene Oxide Hybrid

DOI: 10.1021/acsami.9b10719
ACS Appl. Mater. Interfaces 2019, 11, 35977−35986

Nanolayers for High Performance Asymmetric Supercapacitors with Remarkable Cycling Stability. *ACS Appl. Mater. Interfaces* **2016**, *8*, 1992−2000.
(31) Tian, M.; Li, R.; Liu, C.; Long, D.; Cao, G. Aqueous Al-Ion Supercapacitor with V_2O_5 Mesoporous Carbon Electrodes. *ACS Appl. Mater. Interfaces* **2019**, *11*, 15573−15580.
(32) Bonafede, S. J.; Ward, M. D. Selective Nucleation and Growth of An Organic Polymorph by Ledge-Directed Epitaxy on A Molecular Crystal Substrate. *J. Am. Chem. Soc.* **1995**, *117*, 7853−7861.
(33) Demuth, J.; Fahrenkrug, E.; Maldonado, S. Controlling Nucleation and Crystal Growth of Ge in A Liquid Metal Solvent. *Cryst. Growth Des.* **2016**, *16*, 7130−7138.
(34) Smith, T. F.; Shelton, R. N.; Schwall, R. E.; Clark, A.; Williams, R. H. Related Content A Study of Single-Layer and Restacked MoS_2 by X-Ray Diffraction and X-Ray Absorption Spectroscopy. *J. Phys. C: Solid State Phys.* **1987**, *20*, 4043−4053.
(35) Rao, A. M.; Eklund, P. C.; Bandow, S.; Thess, A.; Smalley, R. E. Evidence for Charge Transfer in Doped Carbon Nanotube Bundles from Raman Scattering. *Nature* **1997**, *191*, 257−259.
(36) Zhang, Z.; Yang, Z.; Huang, J.; Feng, Z.; Xie, X. Enhancement of Electrochemical Performance with Zn-Al-Bi Layered Hydrotalcites as Anode Material for Zn/Ni Secondary Battery. *Electrochim. Acta* **2015**, *155*, 61−68.
(37) Liu, L.; Cheng, M.; Yang, Z. Improved Performance of Flower-Like ZnAl LDH Growing on Carbon Nanotubes Used in Zinc-Nickel Secondary Battery. *Electrochim. Acta* **2018**, *277*, 67−76.
(38) Cao, F. F.; Guo, Y. G.; Wan, L. J. Better Lithium-Ion Batteries with Nanocable-Like Electrode Materials. *Energy Environ. Sci.* **2011**, *4*, 1634−1642.
(39) Wang, S.; Guan, B. Y.; Yu, L.; Lou, X. W. Rational Design of Three-Layered TiO2@Carbon@MoS_2 Hierarchical Nanotubes for Enhanced Lithium Storage. *Adv. Mater.* **2017**, *1702724*, 1−5.
(40) Ng, S. H.; Wang, J.; Guo, Z. P.; Chen, J.; Wang, G. X.; Liu, H. K. Single Wall Carbon Nanotube Paper as Anode for Lithium-Ion Battery. *Electrochim. Acta* **2005**, *51*, 23−28.
(41) Ni, S.; Lv, X.; Li, T.; Yang, X.; Zhang, L. The Investigation of $Ni(OH)_2$/Ni as Anodes for High Performance Li-Ion Batteries. *J. Mater. Chem. A* **2013**, *1*, 1544−1547.
(42) Yuan, T.; Jiang, Y.; Sun, W.; Xiang, B.; Li, Y.; Yan, M.; Xu, B. Ever-Increasing Pseudocapacitance in RGO-MnO-RGO Sandwich Nanostructures for Ultrahigh-Rate Lithium Storage. *Adv. Funct. Mater.* **2016**, *26*, 2198−2206.
(43) Yang, C.; Zhang, Y.; Zhou, J.; Lin, C.; Lv, F.; Wang, K.; Feng, J.; Xu, Z.; Li, Z.; Guo, S. Hollow Si/SiOx Nanosphere/Nitrogen-Doped Carbon Superstructure with A Double Shell and Void for High-Rate and Long-Life Lithium-Ion Storage. *J. Mater. Chem. A* **2018**, *6*, 8039−8046.
(44) Wei, Q.; Wei, Q.; Jiang, Y.; Qian, X.; Zhang, L.; Li, Q.; Tan, S.; Zhao, K. Sodium Ion Capacitor Using Pseudocapacitive Layered Ferric Vanadate Nanosheets Cathode Sodium Ion Capacitor Using Pseudocapacitive Layered Ferric Vanadate Nanosheets Cathode. *iScience* **2018**, *6*, 212−221.
(45) Chao, D.; Zhu, C.; Yang, P.; Xia, X.; Liu, J.; Wang, J.; Fan, X.; Savilov, S. V.; Lin, J.; Fan, H. J.; Shen, Z. X. Array of Nanosheets Render Ultrafast and High-Capacity Na-Ion Storage by Tunable Pseudocapacitance. *Nat. Commun.* **2016**, *7*, No. 12122.
(46) Brezesinski, T.; Wang, J.; Tolbert, S. H.; Dunn, B. Ordered Mesoporous Alpha-MoO_3 with Iso-Oriented Nanocrystalline Walls for Thin-Film Pseudocapacitors. *Nat. Mater.* **2010**, *9*, 146−151.
(47) Chen, Z.; Xu, F.; Cao, S.; Li, Z.; Yang, H.; Ai, X. High Rate, Long Lifespan LiV_3O_8 Nanorods as A Cathode Material for Lithium-Ion Batteries. *Small* **2017**, *13*, 1−9.
(48) Jiang, S.; Dong, S.; Wu, L.; Chen, Z.; Shen, L.; Zhang, X. Pseudocapacitive T-Nb_2O_5/N-Doped Carbon Nanosheets Anode Enable High Performance Lithium-Ion Capacitors. *J. Electroanal. Chem.* **2019**, *842*, 82−88.
(49) Yu, P.; Cao, G.; Yi, S.; Zhang, X.; Li, C.; Sun, X.; Wang, K.; Ma, Y. Binder-Free 2D Titanium Carbide (MXene)/Carbon Nanotube Composites for High-Performance Lithium-Ion Capacitors. *Nanoscale* **2018**, *10*, 5906−5913.
(50) Han, C.; Xu, L.; Li, H.; Shi, R.; Zhang, T.; Li, J.; Wong, C.; Kang, F.; Lin, Z.; Li, B. Biopolymer-Assisted Synthesis of 3D Interconnected Fe_3O_4@Carbon Core@Shell as Anode for Asymmetric Lithium Ion Capacitors. *Carbon* **2018**, *140*, 296−305.
(51) Wang, H.; Zhang, Y.; Ang, H.; Zhang, Y.; Tan, H. T.; Zhang, Y.; Guo, Y.; Franklin, J. B.; Wu, X. L.; Srinivasan, M.; et al. A High-Energy Lithium-Ion Capacitor by Integration of a 3D Interconnected Titanium Carbide Nanoparticle Chain Anode with A Pyridine-Derived Porous Nitrogen-Doped Carbon Cathode. *Adv. Funct. Mater.* **2016**, *26*, 3082−3093.
(52) Kim, H.; Cho, M.; Kim, M.; Park, K.; Gwon, H.; Lee, Y.; Roh, K. C.; Kang, K. A Novel High-Energy Hybrid Supercapacitor with An Anatase TiO_2−Reduced Graphene Oxide Anode and An Activated Carbon Cathode. *Adv. Energy Mater.* **2013**, *3*, 1500−1506.
(53) Kong, L.; Zhang, C.; Zhang, S.; Wang, J.; Cai, R.; Lv, C.; Qiao, W.; Ling, L.; Long, D. High-Power and High-Energy Asymmetric Supercapacitors Based on Li^+-Intercalation into T-Nb_2O_5/Graphene Pseudocapative Electrode. *J. Mater. Chem. A* **2014**, *2*, 17962−17970.
(54) Aravindan, V.; Cheah, L.; Mak, F.; Wee, G. Fabrication of High Energy-Density Hybrid Supercapacitors Using Electrospun V_2O_5 Nanofibers with A Self-Supported Carbon Nanotube Network. *ChemPlusChem* **2012**, *77*, 570−575.
(55) Cao, W. J.; Zheng, J. P. Li-Ion Capacitors with Carbon Cathode and Hard Carbon/Stabilized Lithium Metal Powder Anode Electrodes. *J. Power Sources* **2012**, *213*, 180−185.
(56) Wang, B. Q.; Wen, Z.; Li, J. A Hybrid Supercapacitor Fabricated with A Carbon Nanotube Cathode and A TiO_2−B Nanowire Anode. *Adv. Funct. Mater.* **2006**, *16*, 2141−2146.

DOI: 10.1021/acsami.9b10719
ACS Appl. Mater. Interfaces 2019, 11, 35977−35986